The Triggering of Orographic Rainbands by Small-Scale Topography

DANIEL J. KIRSHBAUM, GEORGE H. BRYAN, AND RICHARD ROTUNNO

National Center for Atmospheric Research,* Boulder, Colorado

DALE R. DURRAN

Department of Atmospheric Sciences, University of Washington, Seattle, Washington

ABSTRACT

The triggering of convective orographic rainbands by small-scale topographic features is investigated through observations of a banded precipitation event over the Oregon Coastal Range and simulations using a cloud-resolving numerical model. A quasi-idealized simulation of the observed event reproduces the bands in the radar observations, indicating the model's ability to capture the physics of the band-formation process. Additional idealized simulations reinforce that the bands are triggered by lee waves past small-scale topographic obstacles just upstream of the nominal leading edge of the orographic cloud. Whether a topographic obstacle in this region is able to trigger a strong rainband depends on the phase of its lee wave at cloud entry. Convective growth only occurs downstream of obstacles that give rise to lee-wave-induced displacements that create positive vertical velocity anomalies w_c and nearly zero buoyancy anomalies b_c as air parcels undergo saturation. This relationship is quantified through a simple analytic condition involving w_c, b_c, and the static stability N_m^2 of the cloud mass. Once convection is triggered, horizontal buoyancy gradients in the cross-flow direction generate circulations that align the bands parallel to the flow direction.

1. Introduction

One simple but common orographic precipitation mechanism involves the ascent of moist low-level air over a hill, where it saturates and produces precipitation (e.g., Houze 1993). When this "cap" cloud is statically unstable, convective structures may develop that influence the rate, efficiency, and fallout of precipitation. Results from observational studies (e.g., Elliott and Hovind 1964; Dirks 1973) and, more recently, numerical studies (Kirshbaum and Durran 2004; Fuhrer and Schär 2005) all suggest that orographic precipitation is enhanced in convective events compared to stratiform events.

In addition to increasing the area-averaged precipitation, orographic convection may take the form of quasi-stationary banded structures that concentrate most of their rainfall over specific locations. Observations of banded orographic precipitation events over the western Kyushu region of Japan (Yoshizaki et al. 2000), the Cévennes region of France (Miniscloux et al. 2001; Cosma et al. 2002), and the Oregon Coastal Range (Kirshbaum and Durran 2005b) have suggested that the steadiness of the bands may lead to daily cumulative precipitation amounts in excess of 100 mm. These studies identified some common ingredients for band formation, including potential instability, high relative humidity, and moderate wind speeds in the upstream flow, along with the presence of small-scale topographic obstacles on the terrain upstream of the ridge crest.

Despite the broad consistencies between the cases cited above, their different terrain geometries and upstream flows led to differences in the structures of the bands. For example, the rainbands in Yoshizaki et al. (2000) were triggered by two widely spaced peninsulas upstream of the Kyushu range, while those in Cosma et al. (2002) formed past closely spaced peaks on the upslope of the Cévennes, and those in Kirshbaum and Durran (2005b) formed not just past small-scale peaks
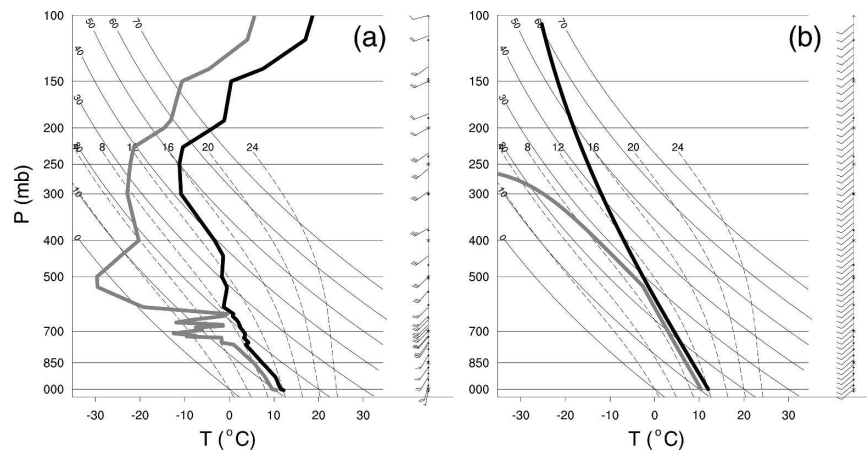
FIG. 1. Real and idealized sounding data. (a) Radiosonde at 0000 UTC 13 Nov 2002 from Quillayute during the Coastal Range orographic precipitation event, and (b) a simplified version of (a) used in the idealized experiments. In these skew T–$\log p$ plots, temperature is the thick black line, dewpoint is the thick gray line, dry adiabats are thin solid lines, moist adiabats are thin dashed lines, and wind barbs with flags at intervals of 10 m s^{-1} are shown to the right.

but also valleys embedded on the Coastal Range upslope. This may help to explain why the bands over western Kyushu were spaced much farther apart (~100 km) than those over the Cévennes and Coastal Range (5–15 km). Moreover, the low-level instability of the flow impinging on western Kyushu was much stronger than that over the Cévennes and the Coastal Range, which may have caused the bands over western Kyushu to be deeper (5–6 km) than those in the other two cases (2–4 km). These differences indicate that structural details of the rainbands may strongly depend on both the flow passing over the mountain and the terrain of the region.

Insight into the atmospheric factors promoting quasi-stationary rainbands over the Coastal Range is provided by the numerical experiments of Kirshbaum and Durran (2005a), who found that marginal potential instability and moderate wind speeds ($\geq$10 m s^{-1}) in the cloud layer were the most favorable atmospheric conditions for bands to develop. Their simulated bands formed equally well in both sheared and unsheared environments, implying that shear was not necessary to organize the convection into elongated bands. The authors hypothesized that the bands were triggered by lee waves induced by small-scale terrain features just upstream of the orographic cloud, past which the air ascended convectively into an updraft band.

As a logical follow-up to Kirshbaum and Durran (2005a), this paper provides an in-depth study of the dynamics by which small-scale terrain obstacles trigger quasi-stationary rainbands over a mesoscale orographic barrier. This is accomplished through a combination of observational and numerical analysis. We first revisit radar observations of a banded convective event over

the Coastal Range in Kirshbaum and Durran (2005b) to illustrate the locations and horizontal structures of the rainbands. We then introduce the cloud-resolving numerical model and perform a quasi-idealized simulation of this event using the real upstream flow and Coastal Range terrain. A series of idealized simulations are then carried out with simpler upstream flows and terrain profiles to identify the physical processes that govern the preferred locations of orographic rainbands.

2. Observations

The three precipitation events over the Oregon Coastal Range studied in Kirshbaum and Durran (2005b) all occurred in postfrontal synoptic environments with upstream flows containing potential instability from the surface to a height of around 3 km. Once lifted to saturation over the Coastal Range, they generated convective structures with various degrees of banded organization and steadiness. The most banded and steady event of the three (case 2 in that paper) occurred over 12–13 November 2002. A representative upstream sounding profile during this event from Quillayute, Washington (about 200 km north of the Coastal Range), at 0000 UTC 13 November 2002 in Fig. 1a is characterized by moderate ($\geq$10 m s^{-1}) southwesterly winds, weak conditional instability (CAPE $\approx$ 500 J), and high relative humidity ($\approx$90%) at low levels.

A representative radar reflectivity image from this event, taken from the Next-Generation Weather Radar (NEXRAD) Portland, Oregon, site at 2003 UTC 12 November 2002, is contoured at 5-dBZ intervals in Fig. 2a. These data were obtained from a 0.5° elevation radar scan whose upward-pointing beam reaches a physi-
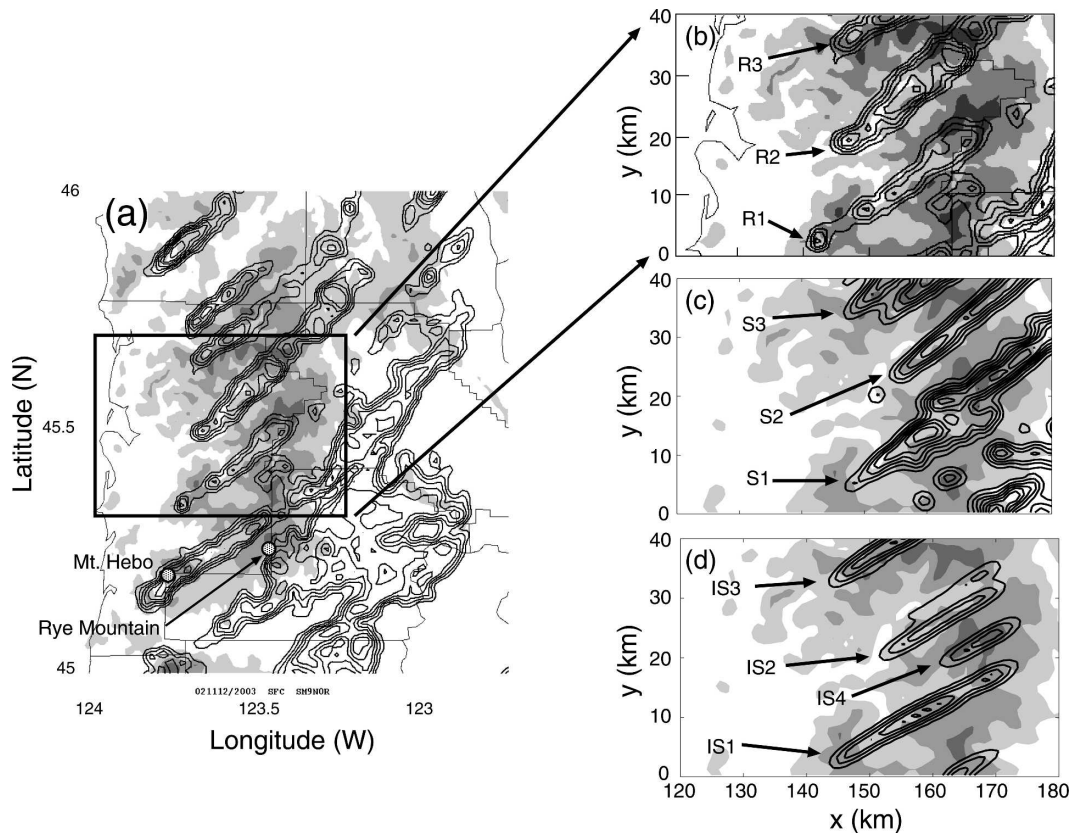
FIG. 2. Comparison between radar observations and simulated reflectivity fields. (a) Radar reflectivity field at 2003 UTC 12 Nov 2002 over Coastal Range, (b) cropped image of (a) over study area, (c) simulated reflectivity from CTL simulation, and (d) simulated reflectivity from IDEAL simulation. Grayscale topographic contours are in intervals of 250 m and overlaid reflectivity lines are contoured in intervals of 5 dBZ.

cal height of approximately 1.5 km in the center of the figure. A nine-point spatial filter has been applied that smoothes the contours and decreases the effective horizontal resolution of the radar data above its nominal value of 1 km. Remarkably well organized rainbands are apparent over the mountain upslope that persisted in the same locations for the duration of this event. The upstream edges of these bands are located not directly over the ridge peak at approximately 123.5°W but rather far upstream of it. Although some of the bands in Fig. 2a appear to form over and downstream of small-scale peaks on the gradually sloping barrier, others form past valleys or have no clear connection to obvious small-scale features. The steadiness of these rainbands led to highly variable precipitation accumulations, with Mt. Hebo recording 69 mm in just 6 h and Rye Mountain, located just 20 km to the east but not directly under a band, recording only 8 mm over the same interval. For more details on the structures of these rainbands, or those in other events over the Coastal Range, the reader is referred to Kirshbaum and Durran (2005b).

3. A quasi-idealized simulation of the event

The numerical model used for all the simulations is cloud resolving, nonhydrostatic, and fully nonlinear, with governing equations described in Bryan and Fritsch (2002). Solutions to these equations are achieved using a split time step technique to maintain stability of acoustic modes (Klemp and Wilhelmson 1978), with the acoustic terms treated explicitly in the horizontal direction and implicitly in the vertical. Integration of variables on the larger time step is performed using the Runge–Kutta technique formulated for compressible models by Wicker and Skamarock (2002). Advection is performed with a centered sixth-order scheme, and sixth-order artificial diffusion is applied to all variables in the horizontal direction. Microphysical processes are parameterized through a warm rain Kessler scheme (e.g., Klemp and Wilhelmson 1978), and subgrid-scale turbulence is parameterized using Smagorinsky-type first-order closure (e.g., Lilly 1962). The experimental domain has dimensions of $L_x \times L_y \times L_z$, with a free-slip lower boundary and the uppermost
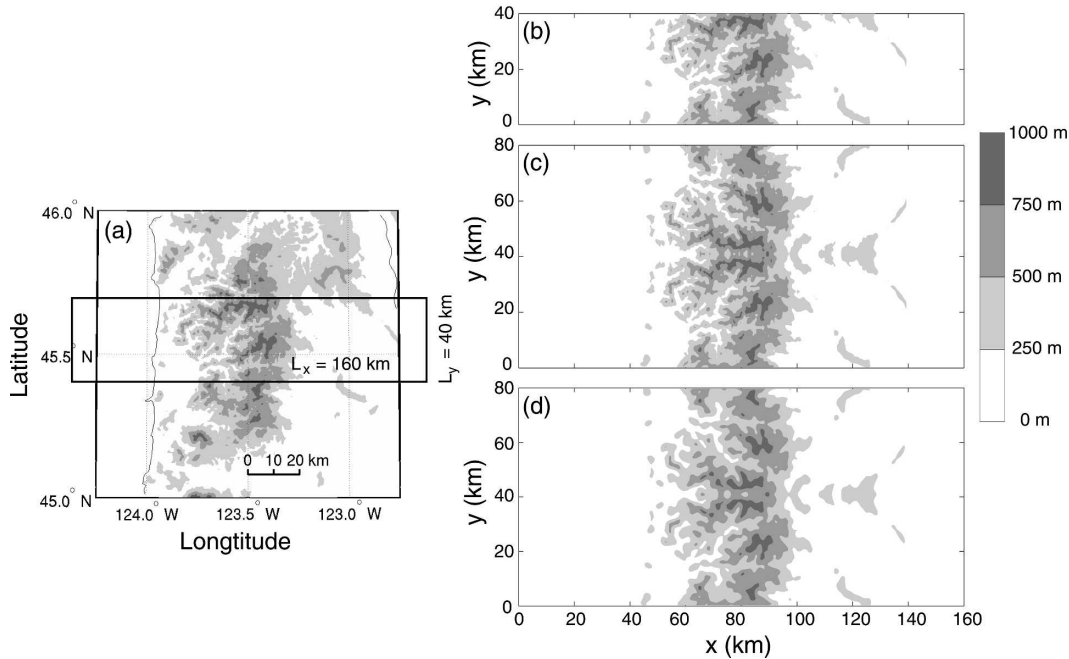
FIG. 3. Topography of northwestern Oregon. (a) Raw data imported from Gtopo30 at 1/120° resolution; (b) 160 km × 40 km section of topography [corresponding to the boxed area in (a)] interpolated to Cartesian grid with $\Delta_h = 500$ m; (c) same as in (b), but with topography from $0 \le y \le 40$ mirrored over $40 < y \le 80$ km; and (d) same as in (c), but with $6\Delta x$ filter applied.

5 km in z serving as a Rayleigh damping layer to absorb vertically propagating waves. Lateral boundary conditions are periodic in y and outflow in x using a one-way wave equation (e.g., Durran and Klemp 1983) with a constant phase speed of 25 m s^{-1}. Rotational effects are neglected due to the high characteristic Rossby numbers of the flows under consideration, and ice processes are neglected because the cloud tops in these simulations generally do not extend far above the freezing level.

The study area for this analysis, shown by the box in Fig. 3a, is a quasi-2D section of the northwestern Oregon Coastal Range terrain downloaded from the U.S. Geological Survey's (USGS) Global 30 Arc-Second Elevation Dataset (Gtopo30) global elevation model with a resolution of 1/120°. To prepare this terrain map for use in the model, it is first linearly interpolated to a Cartesian grid whose centerpoint lies along the main ridge axis at 45.4°N and 123.5°W (Fig. 3b). This grid has a horizontal spacing of $\Delta_h = \Delta x = \Delta y = 500$ m, which is similar to the nominal Gtopo30 resolution, and a size of 160 km × 40 km. Periodicity in the y direction is achieved by adding a mirror image of the terrain over $40 < y \le 80$ km, which sets $L_y = 80$ km (Fig. 3c). The topography is then low-pass filtered to remove all variance at horizontal scales less than $6\Delta_h$ that are poorly resolved by the numerical model (Fig. 3d). Finally, to

minimize the potential spurious effects of gravity wave reflection at the outflow x boundaries, we expand the domain to $L_x = 320$ km while keeping the ridge axis positioned at its center ($x = 160$ km).

The numerical model's ability to reproduce observed convective features is evaluated through a quasi-idealized simulation, hereafter called CTL, of the 12–13 November precipitation event over western Oregon. For this simulation we use the periodic Coastal Range terrain in Fig. 3d and an upstream flow that is identical to that in Fig. 1a, except that the winds have been rotated clockwise by 10° to account for mesoscale variations in wind direction between Quillayute and the Coastal Range apparent from reanalysis data of this event (not shown). The numerical grid has a horizontal spacing of $\Delta_h = 500$ m and a variable vertical spacing that is $\Delta z = 125$ m at low levels ($z \le 5$ km), stretches to 500 m over $5 < z \le 10$ km, and remains constant at 500 m to the top of the domain at $L_z = 15$ km. Approximately 2 h of integration time are needed for the flow to become quasi-steady, and we display output fields at the final integration time of $t = 4$ h. Horizontal cross sections of this simulation, and all subsequent simulations, are shown at a height of $z = 1.5$ km that is similar to the 0.5° beam height that the Portland radar reaches over the western slopes of the Coastal Range.

In Figs. 2b,c the observed radar reflectivities over the

study area are directly compared to simulated reflectivities from the CTL simulation over $0 \leq y \leq 40$ km.[1] For consistency the simulated reflectivities in Fig. 2c are first smoothed to the nominal radar resolution of 1 km, then filtered by the same nine-point operator that was applied to the radar data. The three stationary bands in the simulation (S1, S2, and S3 in Fig. 2c) are clearly in the same locations over the upslope as those in the radar data (R1, R2, and R3 in Fig. 2b), though with slight differences in the intensity and width of each band. Discrepancies among these finer details are not surprising, considering that the idealized setup of the simulation neglects or simplifies numerous physical processes that may contribute to the observed reflectivity pattern. Nonetheless, the strong agreement in the band locations between the observations and the simulation suggests that this idealized numerical approach is able to accurately capture the primary subject of this study—the physics that control the triggering, and hence the locations, of the rainbands.

4. Idealized simulations

Having demonstrated that the numerical model provides a reasonable solution for a given test case, we now use the model as a tool to investigate the dynamics behind the orographic rainbands. To this end, we perform a series of simulations that are progressively simplified until the physical processes behind rainband triggering are easily identified.

a. Simplifying the upstream flow

As a first step in the idealization process, we perform a simulation named IDEAL that is identical to the CTL case except for the use of the idealized sounding in Fig. 1b. This sounding is designed to capture the gross low-level features of the observed sounding while greatly simplifying the atmospheric structure so that it is defined by just a few parameters. The winds are simplified by setting their magnitude $|\mathbf{U}| = U = 10$ m s^{-1} and direction $\angle \mathbf{U} = \Theta = 230°$ (measured clockwise from due north) to uniform values representative of the low-level conditions in the real sounding. Similarly, thermodynamic conditions at the surface ($T_s = 285$ K; RH$_s = 90\%$) are identical in both soundings, but in the idealized case the square of the dry Brunt–Väisälä frequency

is set to a uniform value ($N_d^2 = 1 \times 10^{-4}$ s^{-2}) and relative humidity is given by a piecewise linear function of height with constant values of RH = 90% at the surface and RH = 1% aloft with a linear transition zone over $5 \leq z \leq 10$ km. Note that this idealized sounding neglects the vertical shear as well as the stable layers aloft between 600 and 400 mb and above the tropopause at 225 mb in the real sounding (Fig. 1a).

Despite the simplifications made to its upstream flow, the IDEAL simulation develops organized rainbands at similar locations (IS1, IS2, and IS3 in Fig. 2d) as in the CTL case (S1, S2, and S3 in Fig. 2c). These bands form in the absence of any basic-state vertical shear, which supports the argument of Kirshbaum and Durran (2005a) that shear is not necessary for band formation, and in some cases may actually hinder it. In particular, directional shear was found to partially suppress rainbands triggered by small-scale topographic features, which lost their vertical coherence when the wind direction turned with height. This may explain the one extra band (labeled IS4 in Fig. 2d) in the IDEAL simulation that was not present in the CTL case. This relatively weak and short band may have been suppressed by the low-level directional shear in the CTL sounding (Fig. 1a) but is able to emerge in the unsheared IDEAL sounding (Fig. 1b).

A second idealization is to rotate the basic-state wind vector from $\Theta = 230°$ to $\Theta = 270°$ so that it is oriented purely from the west. This wind rotation not only aligns the flow with the grid axes, but it demonstrates the influence of wind direction on band alignment. Horizontal cross sections of cloud water (q_c) from the IDEAL simulation (Fig. 4a) and the TH270 simulation (Fig. 4b), which is identical except for using this rotated wind field, indicate that the cloud bands in this case rotate in phase with the 40° mean wind rotation, suggesting that their alignments are parallel to the flow direction. Two vertical x–z cross sections of vertical velocity (w) and q_c taken through a band ($y = 15$ km) and between bands ($y = 12$ km) in Fig. 4b are shown in Figs. 4c,d. In both cases a cloud forms in an elevated, upstream-tilted region of positive vertical motion past small-scale terrain obstacles near $x = 125$ km, yet a strong rainband only forms at $y = 15$ km, not at $y = 12$ km. Although a cloud is evident at $y = 12$ km, its vertical motion does not intensify with distance downstream like the updraft at $y = 15$ km.

b. Simplifying the terrain

The influence of small-scale topographic features on orographic convection may be more straightforwardly examined through simulations with simpler terrain than that of the Coastal Range. To create idealized terrain

---

[1] The conversion algorithm is provided by Douglas (1964): $Z = 2.4 \times 10^4 (\rho_{dry} q_r)^{1.82}$, where $\rho_{dry} = (p - e^*)/(R_d T)$, T is the air temperature, R_d the specific gas constant for dry air, p the air pressure, e^* is the saturation vapor pressure of water at T, and q_r is the rainwater mixing ratio.
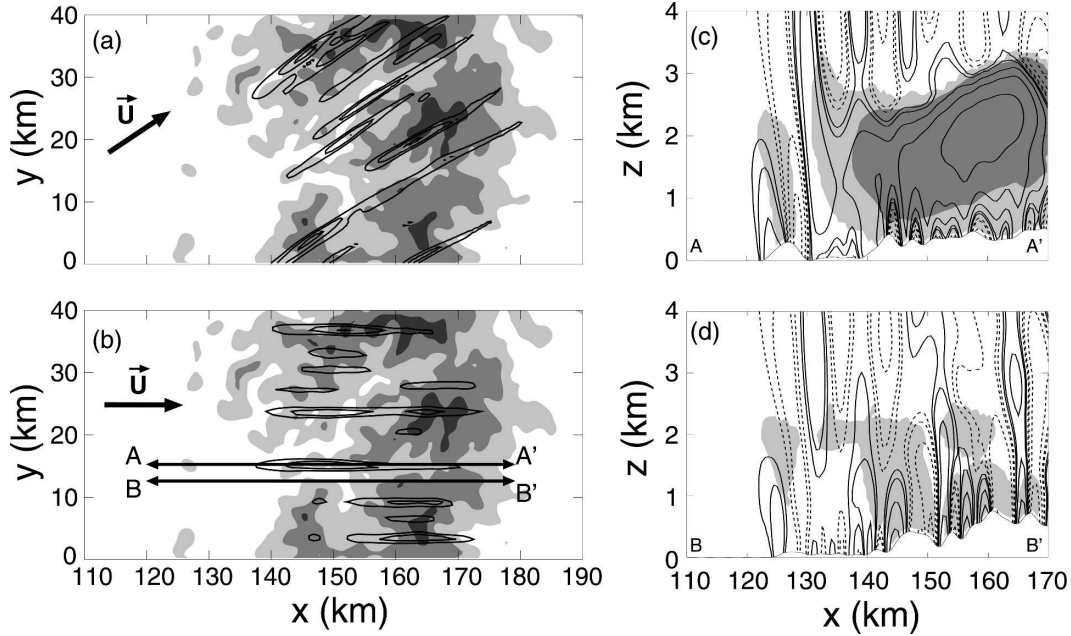
FIG. 4. Comparison between CTL and TH270 simulation, as well as vertical slices through the TH270 simulation. Cloud liquid water field at $t = 4$ h and $z = 1.5$ km overlying shaded topography in 250-m intervals of (a) CTL simulation and (b) TH270 simulation. Contours of q_c are in intervals of 0.4 g kg^{-1}. (c) Vertical cross sections of ω (thin lines, solid for $\omega > 0$, and dashed for $\omega < 0$) and q_c (0.001 and 0.4 g kg^{-1}) along line A–A′ at $y = 15$ km and (d) along line B–B′ at $y = 12$ km. Contours of ω are -1, -0.5, -0.2, -0.1, 0.1, 0.2, 0.5, 1, and 2 m s^{-1}.

representations, we decompose the Coastal Range terrain h into a mesoscale or "mean" component $\overline{h}$ and a small-scale or "perturbation" component $\tilde{h}$, the sum of which is equal to h. This multiscale decomposition is advantageous in that it allows for a systematic separation between the broader mesoscale lifting of the mountain ridge and the embedded smaller-scale topographic obstacles that trigger the convection. This is accomplished by taking the discrete Fourier transform of h:

$$\hat{h}(k_x, k_y) = \frac{1}{N_x N_y} \sum_{n_i=1}^{N_x} \sum_{n_j=1}^{N_y} h(n_i \Delta x, n_j \Delta y) e^{-2\pi i \{[(k_x-1)(n_i-1)/N_x] + [(k_y-1)(n_j-1)/N_y]\}}, \tag{1}$$

where N_x and N_y are the number of grid points in the x and y directions, then defining $\hat{\overline{h}}$ as a 1D spectrum containing all Fourier components with $k_y = 1$ and

$$k_x \leq 1 + \frac{L_x}{\lambda_h}, \tag{2}$$

where $\lambda_h = 40$ km is the minimum wavelength in $\hat{\overline{h}}$ and $\hat{\tilde{h}}$ as all the remaining components. Inverse Fourier transforms of $\hat{\overline{h}}$ and $\hat{\tilde{h}}$ yield the $\overline{h}$ and $\tilde{h}$ fields in physical space shown in Figs. 5a,b. The mesoscale terrain $\overline{h}$ (Fig. 5a) is a slowly varying ridge whose height depends only on x, and the small-scale terrain $\tilde{h}$ (Fig. 5b) is a random-looking collection of small hills and valleys.

The vertical cross sections in Figs. 4c,d suggest that the small-scale terrain just upstream of the orographic cloud edge causes flow perturbations that intersect the cloud and influence the moist dynamics farther downstream. The extent to which the terrain over this limited area controls the overall convective response is examined by a simulation (TH270-PA) that is identical to the TH270 simulation except that $\tilde{h} = 0$ everywhere except for $40 < x < 60$ km, leaving only a narrow patch of topographic variability well upstream of the ridge crest. The q_c field of this simulation in Fig. 6a reveals that the convective pattern in the TH270 case (Fig. 4b) is virtually unchanged when most of $\tilde{h}$ is removed in the TH270-PA simulation. Similarly, vertical cross sections of the TH270-PA simulation, taken through a band at $y = 15$ km (Fig. 6b) and between two bands at $y = 12$ km (Fig. 6c), exhibit similar vertical velocity patterns and cloud extent as the TH270 case (Figs. 4c,d). This comparison suggests that, for a given mesoscale terrain
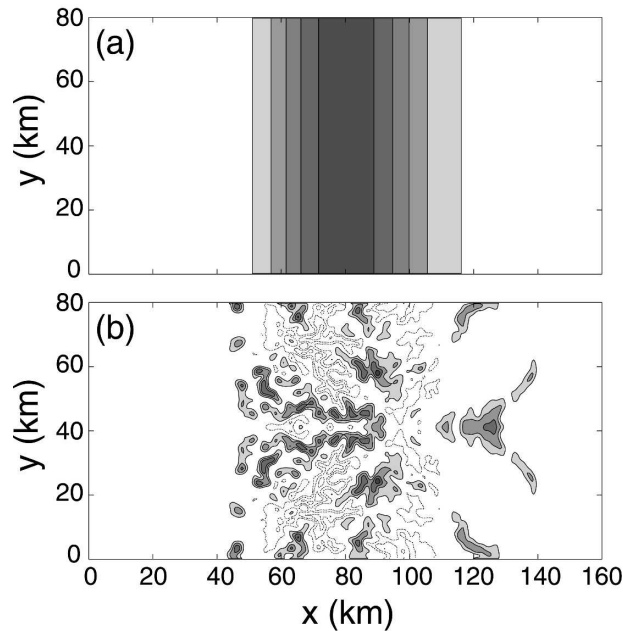
FIG. 5. Decomposition of Coastal Range topography into (a) $\bar{h}$ and (b) $\tilde{h}$. Filled contours of positive topography are in intervals of 100 m. Dashed unfilled contours in (b) are negative topography, also contoured at 100-m intervals.

profile $\bar{h}$, the small-scale terrain $\tilde{h}$ over a small area on the mountain upslope may dictate the convective response over the entire mountain.

The flow response in the complete absence of $\tilde{h}$ is examined by a simulation (NoHs) in which $\tilde{h}$ is zero everywhere. Since the terrain resolution is no longer limited by that of the Gtopo30 dataset, we increase the numerical resolution of this simulation, and all of those to follow, by decreasing Δ_h to 250 m. To minimize the added computational expense associated with this higher resolution, we decrease L_x and L_y by a factor of 2 (to 160 and 20 km, respectively, with the domain still centered around the terrain centerpoint). Note that, because $\bar{h}(x)$ is 1D and the domain is periodic, the reduced width of the domain has no influence on the basic flow response in this case.

The horizontal cross section of q_c in the NoHs simulation in Fig. 7a demonstrates that, in contrast to the previous simulations with nonzero $\tilde{h}$, convection does not occur. The flow exhibits no perceptible y variability and is essentially 2D, varying only in x and z. A vertical cross section of the cloud outline and static stability (N^2 in dry regions, N_m^2 in saturated regions) at $y = 10$ km indicates that virtually all of the cloud possesses moist instability ($N_m^2 < 0$), yet little to no convection develops within it. In the absence of $\tilde{h}$ or any other small-scale forcing mechanism, little to no energy is projected onto rapidly growing small-scale convective modes and, as a result, the residence times of air parcels within the cap cloud is too short to allow noticeable convection to develop from numerical round-off errors alone (Kirshbaum and Durran 2004).

c. A single small-scale feature

The complicated $\tilde{h}$ fields in the TH270 and TH270-PA simulations are collections of many Fourier modes
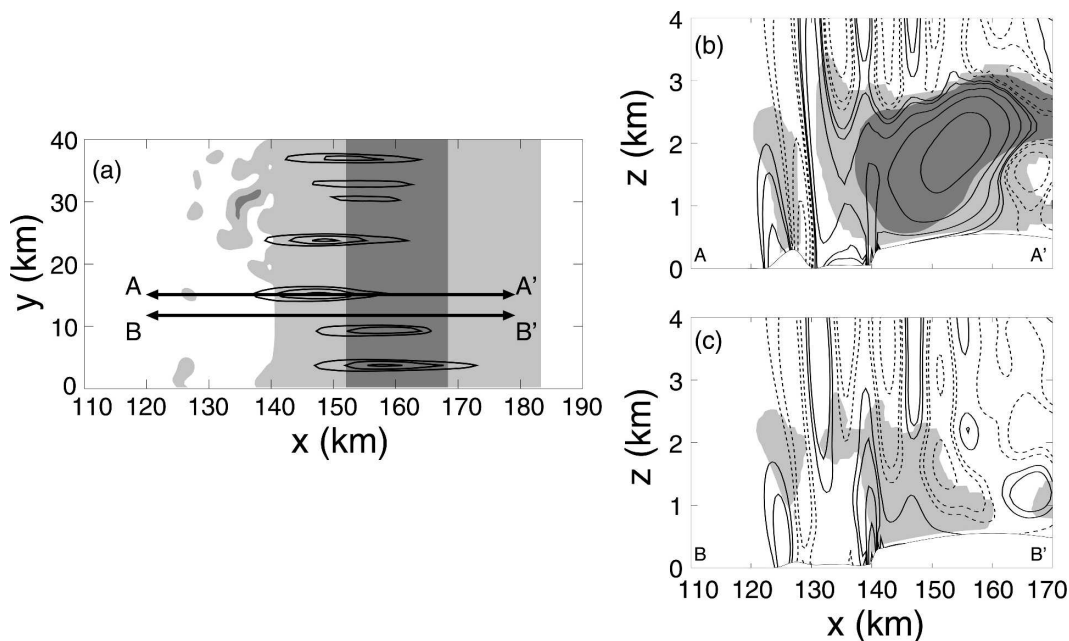

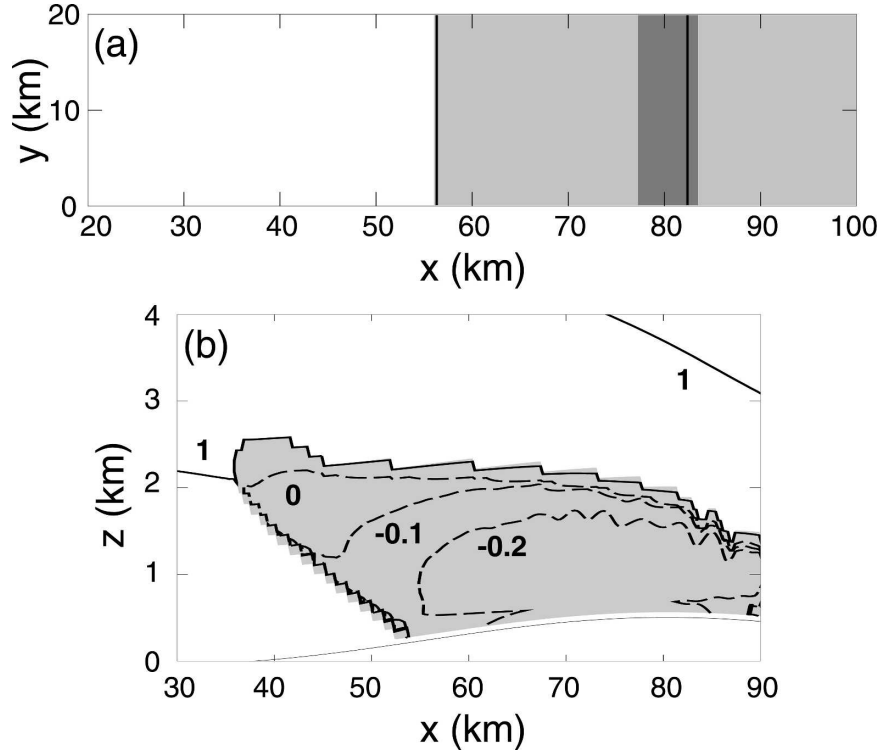FIG. 6. Same as in Figs. 4b–d but for TH270-PA simulation.

FIG. 7. Cross sections of NoHs simulation. (a) Cloud water q_c at 0.1 g kg^{-1} overlying shaded topography at 250-m intervals at $t = 4$ h and $z = 1.5$ km. (b) Squared Brunt–Väisälä frequency in solid lines for positive values and dashed for negative values, with labeled contour values multiplied by 10^{-4} s^{-2}. Cloud outline, as estimated by 0.001 g kg^{-1} contour, is shaded.

with different amplitudes and phases across a wide spectrum of wavenumbers. The influence of these forcing spectra on the convective response of the flow is also a complicated issue and is deferred to a follow-on study. Here we restrict our focus to the triggering of orographic rainbands, the dynamics of which may be understood using much simpler $\tilde{h}$ fields. The influence of an isolated topographic feature is evaluated by two simulations (HILL and VALLEY) that are identical to the NoHs case except that $\tilde{h}$ is given by

$$\tilde{h}(x, y) = \begin{cases} h_b \cos\left[\dfrac{2\pi}{\lambda_b}(x - x_b)\right] \cos\left[\dfrac{2\pi}{\lambda_b}(y - y_b)\right] : |x - x_b|, |y - y_b| < \lambda_b/4 \\ 0 : \text{otherwise} \end{cases}, \qquad (3)$$

which produces a hill in the HILL simulation ($h_b > 0$) and a valley in the VALLEY simulation ($h_b < 0$). The parameters $\lambda_b = 10$ km, $|h_b| = 100$ m, $x_b = 40$ km, and $y_b = 10$ km are chosen so that the feature possesses an amplitude and scale consistent with prominent individual features in the $\tilde{h}$ field in Fig. 5b and is centered in the domain near the upstream edge of the orographic cloud in the NoHs simulation (Fig. 7b), the region that controls the convective response over the ridge.

The sensitivity of the cloud patterns in the HILL and VALLEY simulations to the topographic obstacles at $x = 40$ km is demonstrated in the q_c plots in Figs. 8a,b.

The HILL simulation (Fig. 8a) develops a strong cloud band downstream of the isolated hill, with desaturated regions surrounding it. Although this result suggests that bands tend to form in the lee of small-scale hills, the VALLEY simulation (Fig. 8b) reveals that bands may also form downstream of a valley. Three bands are evident in this case: a weak band just downstream of valley at $y = 10$ km and two stronger bands surrounding it.

The differences between the HILL and VALLEY simulations are highlighted in Figs. 8c,d, which, like Figs. 4c,d and 6b,c, show vertical cross sections of w and
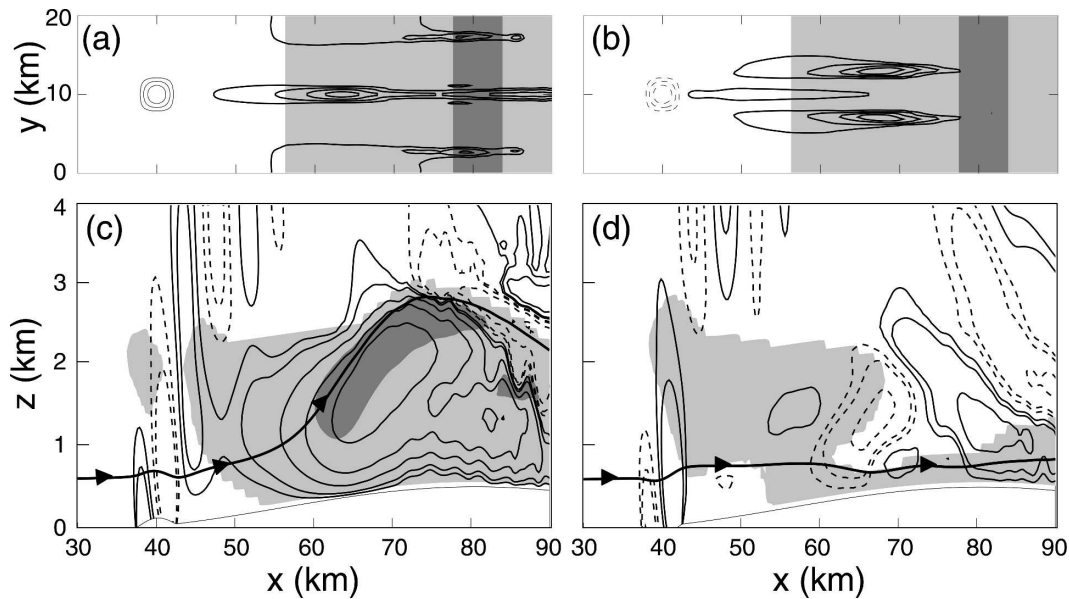
FIG. 8. Horizontal cross sections of q_c at $z = 1.5$ km of (a) HILL and (b) VALLEY simulations. Vertical cross sections at $y = 10$ km of ω, cloud outline, and the forward trajectory of parcel originating at $z = 562.5$ m of (c) HILL and (d) VALLEY simulations. Grayscale topography in (a), (b) is contoured at 250-m intervals, with $\tilde{h}$ also contoured by lines at 25-m intervals (solid for positive values, dashed for negative values). The q_c contours in (a), (b) are the same as in Fig. 4a, and the ω and q_c contours in (c), (d) are the same as in Figs. 4c,d.

q_c past the terrain obstacles at $y = 10$ km. In addition, the streamlines of parcels originating at $z = 562.5$ m are overlaid on the plots to indicate the different paths that near-surface parcels take through the clouds (because the flow is quasi-steady, these streamlines are nearly equivalent to trajectories and we henceforth use the latter term to describe them). Despite the much simpler $\tilde{h}$ fields in these cases, the dynamics of the bands and the nonbanded areas appear qualitatively similar to those in the TH270 and TH270-PA simulations (Figs. 4c,d and 6b,c). In Fig. 8c an oscillating vertical velocity pattern is evident prior to saturation, in which the parcel first rises over the hill, descends past it, and then rises again. Saturation occurs in the ascending air parcel at $x \approx 47$ km, beyond which it gains q_c as it rises convectively to the top of the cloud layer. The vertical velocity pattern near $x \approx 40$ km in the VALLEY simulation differs in sign from that in the HILL case but has approximately the same amplitude. As a consequence saturation occurs farther upstream at $x \approx 42$ km; the vertical motion is weak in the saturated region and the parcel does not rise convectively.

d. A sinusoidal column

Although simulations with a single obstacle provide useful insight into the formation of one or more orographic rainbands, real orographic flows tend to have multiple small-scale terrain features capable of gener-

ating rainbands (e.g., Fig. 2a). Here we take a first step in exploring the influence of multiple topographic features on orographic rainbands by representing $\tilde{h}$ as a column of hills and valleys that extend across the width of the domain. This is implemented by defining $\tilde{h}$ by the 2D cosine wave in (3) except that, rather than being zero for $|y - y_b| > \lambda_b/4$, it spans L_y with two full wavelengths. As in the HILL simulation, $h_b = 100$ m and $y_b = 10$ km so that a small-scale hill lies at the y centerpoint of the domain. The value of $\lambda_b = 10$ km, which is representative of the y distance between the strongest convective bands apparent in the radar observations of the 12–13 November precipitation event (Fig. 2a), is also unchanged.

The q_c fields of three simulations with sinusoidal columns of $\tilde{h}$ at $x_b = 20$ km (Xb20), $x_b = 40$ km (Xb40), and $x_b = 60$ km (Xb60) in Figs. 9a–c reinforce the idea that the convective response depends on the location of the terrain perturbations. Two bands form over the mountain upslope in each case, with the longest bands forming past the two small-scale valleys in the Xb20 case (Fig. 9a), strong but shorter bands forming past the two hills in the Xb40 case (Fig. 9b), and very weak, short bands again forming past the two hills in the Xb60 case (Fig. 9c). This comparison demonstrates that bands may form past either hills or valleys depending on the position of $\tilde{h}$. The relative impacts of the different $\tilde{h}$ fields in the Xb20, Xb40, and Xb60 simulations
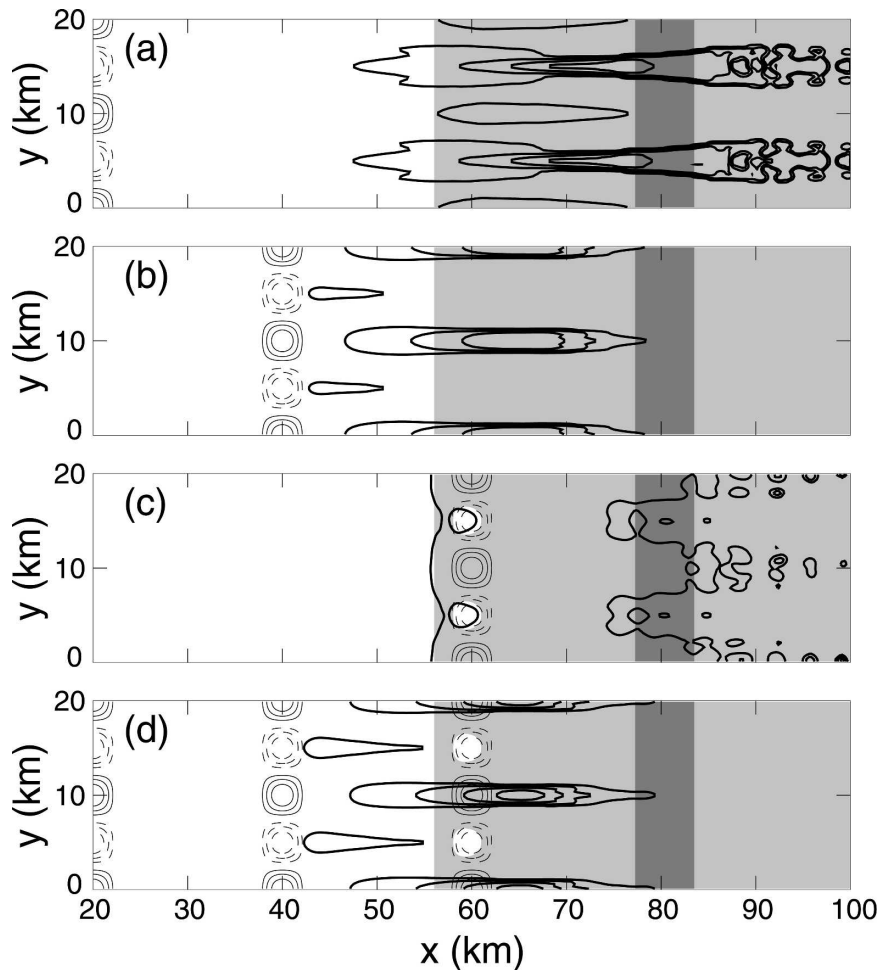
FIG. 9. Cloud water q_c of (a) Xb20, (b) Xb40, (c) Xb60, and (d) 3Xb simulations at $t = 4$ h and $z = 1.5$ km. Contours of q_c are the same as in Fig. 4a. Shaded contours of h are in intervals of 250 m. The small-scale topography $\tilde{h}$ is shown in 25-m contour intervals, with positive values in solid lines and negative values in dashed lines.

are assessed in a fourth simulation (3Xb) that superposes the $\tilde{h}$ fields of all three of these cases so that sinusoidal columns are present at $x = 20, 40$, and 60 km. The two bands apparent in the q_c field in Fig. 9d bear the closest resemblance to those in the Xb40 case (Fig. 9b), suggesting that the column of $\tilde{h}$ at $x_b = 40$ km dominates the convective triggering. This result is consistent with the TH270 and TH270-PA simulations, in which the noise field over a limited area just upstream of the cloud leading edge dictated the overall convective response.

To isolate the flow response to the dominant hills at $x_b = 40$ km, a vertical cross section of w, q_c, and the trajectory of a parcel originating at $z = 562.5$ m in the Xb40 simulation is shown at $y = 10$ km in Fig. 10a. A pattern of fluctuating velocity perturbations reminiscent of the HILL simulation (Fig. 8c) is apparent near

the band leading edge. Moreover, a vertical cross section plotting the same fields past the valleys at $y = 15$ km in Fig. 10b resembles the $y = 10$ km cross section in the VALLEY simulation (Fig. 8d). In the upcoming section we examine the dynamical processes that explain these velocity fluctuations and the reasons why bands form past certain obstacles and not others.

5. Dynamics of the rainbands

The region of $\tilde{h}$ that appears to dominate the convective response in the simulations discussed thus far lies just upstream of the nominal leading edge of the orographic cloud. Over this area, the combination of large-scale ascent induced by $\bar{h}$ and small-scale flow perturbations arising from $\tilde{h}$ lead to saturation, and in some locations, band formation. Preliminary insight
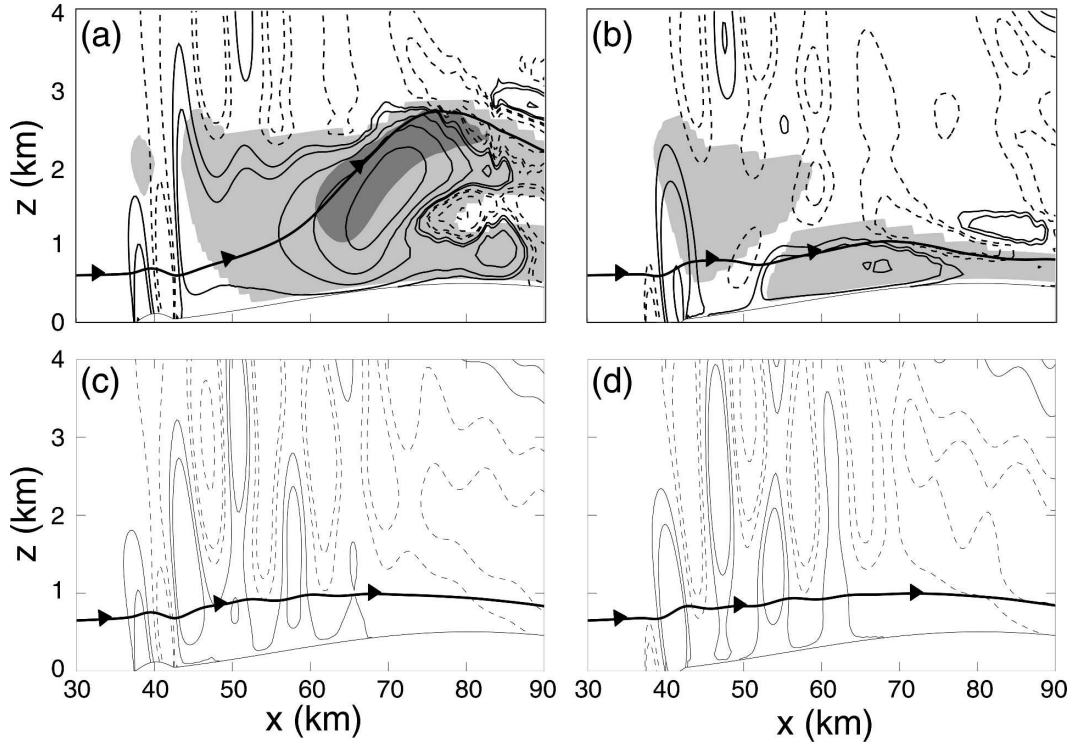
FIG. 10. Vertical cross sections of ω and q_c of the Xb40 simulation at (a) $y = 10$ km and (b) $y = 15$ km. Contours of w and q_c are the same as in Fig. 4c,d. Arrowed lines overlaid on the two panels are forward trajectories of air parcels that originate at $z = 562.5$ m. (c), (d) Same as in (a), (b) but for moisture-free Xb40-DRY simulation.

into this process was provided by Kirshbaum and Durran (2005a), who compared a convective, banded simulation with its dry ($q_v = 0$) counterpart and found that small-scale lee waves in the unsaturated flow upstream of the orographic cloud tended to trigger rainbands when their ascending branches intersected the leading edge of the cloud.

The importance of lee waves in triggering convection is demonstrated in Figs. 10c,d, which show w, q_c, and parcel trajectories of a simulation (Xb40-DRY) that is identical to the Xb40 case except that RH = 0, which precludes the formation of clouds and convection. The oscillating patterns of upward motion upstream of the clouds in the Xb40 simulation still exist in Figs. 10c,d, suggesting that they are a stable response of the flow to $\tilde{h}$. Thus, the cloud at $y = 10$ km in the Xb40 simulation is triggered in an elevated lee-wave updraft at $x \approx 47$ km (Figs. 10a,c) and the cloud at $y = 15$ km is triggered in a lee-wave updraft at $x \approx 42$ km (Figs. 10b,d).

Because the strong bands in the Xb40 simulation form downstream of lee-wave updrafts past the hills at $y = 0$, $y = 10$ km, and $y = 20$ km but not past the valleys at $y = 5$ km and $y = 15$ km, additional dynamics beyond the lee-wave vertical velocity patterns in Fig. 10 must be considered to explain why bands are favored past cer-

tain topographic features and not others. Another variable strongly tied to band formation is buoyancy b, which is given by the following expression (e.g., Durran and Klemp 1982):

$$b = -\int_0^\zeta N^2 \, d\zeta', \qquad (4)$$

where ζ is the vertical displacement of an air parcel along its trajectory and N^2 is the local value of the squared Brunt–Väisälä frequency. Note that (4) is nonlinear because N^2 is not a constant but a variable that depends on whether the parcel is saturated. The consistency between (4) and the simulated buoyancy fields may be examined by substituting ζ along parcel trajectories (Figs. 8c,d and 10c,d) and representative values of $N^2(N_d^2 = 1 \times 10^{-4}\ \text{s}^{-2})$ in unsaturated areas and $N_m^2 = -1.5 \times 10^{-5}\ \text{s}^{-2}$, estimated from Fig. 7b, in saturated areas from the HILL, VALLEY, and Xb40 simulations into (4). Values of b computed through this procedure (not shown) are within 1% of those found directly from the simulation, implying that this equation explains the buoyant forces responsible for the vertical acceleration of air parcels in the simulations. These buoyant forces create flow-parallel banded circulations
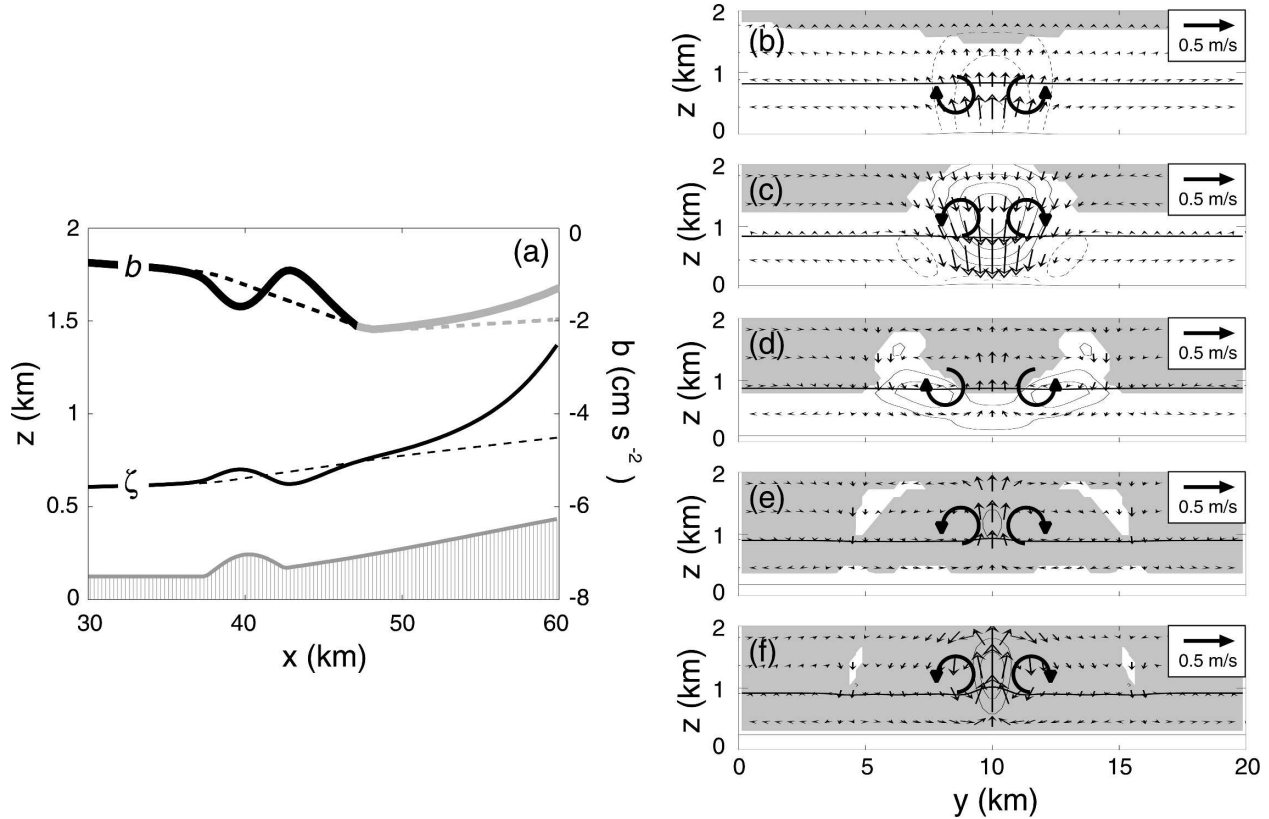
FIG. 11. Dynamical analysis of HILL simulation, showing (a) ζ (thin, lower section) and b (thick, upper section) curves at $y = 10$ km (solid lines) and $y = 0$ (dashed lines). Portions of the b curves in black (gray) correspond to unsaturated (saturated) flow. Underlying topography is shown for illustrative purposes and is not to scale. Cross sections in the y–z plane of cloud outline (shaded), b' (thin lines, solid for $b' > 0$, and dashed for $b' < 0$), plane-parallel velocity vectors (arrows), and heights of parcels originating at $z = 562.5$ m (solid quasi-horizontal line) at (b) $x = 38$ km, (c) $x = 42$ km, (d) $x = 47$ km, (e) $x = 52$ km, and (f) $x = 56$ km. Vorticity tendency directions in (b)–(f) are shown by thick semicircles with arrows.

through the generation of $x -$ vorticity ξ, which in linearized form is given by

$$U\frac{\partial \xi}{\partial x} = U\frac{\partial}{\partial x}\left(\frac{\partial w}{\partial y} - \frac{\partial v}{\partial z}\right) = \frac{\partial b}{\partial y}, \qquad (5)$$

and it is assumed that the flow is steady ($\partial/\partial t = 0$). In the following we use (4) and (5) to explain the origin of the buoyancy-driven convective circulations apparent in the simulations.

a. HILL simulation

The dynamics of air parcels in the HILL simulation are illustrated in Fig. 11a, which plots the values of ζ (thin lines, bottom section) and b (heavy lines, top section) along two different parcel trajectories in the x–z plane. One parcel at $y = 10$ km (solid lines) travels over the small-scale hill and the other at $y = 0$ (dashed lines) is far enough from the hill to be virtually unaffected by its presence, representing the laminar "reference" flow response in the absence of $\tilde{h}$. The b lines are black

where the parcels are unsaturated ($N^2 = N_d^2 > 0$) and gray where they are saturated ($N^2 = N_m^2 < 0$). Considering first the unperturbed parcel at $y = 0$, monotonically increasing displacement occurs throughout its trajectory over $30 \leq x \leq 60$ km. Because the parcel displacement and stability are positive prior to saturation, it accumulates negative buoyancy through (4) until it reaches saturation at $x = 47$ km. An abrupt shift in $\partial b/\partial x$ from negative to positive in Fig. 11a occurs at saturation because the sign of N^2 changes from positive to negative, which reverses the phase relationship between b and ζ in (4) so that the saturated parcel starts to gain buoyancy as it continues to ascend.

Until encountering the hill at $x = 40$ km, the parcel at $y = 10$ km in Fig. 11a behaves similarly to the reference parcel at $y = 0$. As it ascends over the hill ($36 < x < 39$ km), it accumulates positive ζ and negative b relative to the reference parcel. For convenience we henceforth denote all departures from properties of the reference state at $y = 0$ as the perturbation fields ζ', b', etc.,

which allows the 3D perturbations associated with $\tilde{h}$ to be separated from the larger-scale 2D signature associated with $\bar{h}$. Note that this subtraction operation has no influence on y gradients (e.g., $\partial b'/\partial y = \partial b/\partial y$). Returning to Fig. 11a, b' is clearly negative over the hill, which is also seen in the y–z cross section of b' and plane-parallel perturbation velocities (v' and w') at $x = 38$ km in Fig. 11b. This implies $\partial b'/\partial y < 0$ on the south side of the hill and $\partial b'/\partial y > 0$ on the north side, which from (5) tends to decrease ξ on the south side and increase it on the north side (as suggested by the ξ-tendency arrows overlaid on the figure). In a manner that is characteristic of gravity wave oscillations, these counterrotating vorticity tendencies oppose the topographically forced circulation and reverse its direction, which leads to downward motion and increasing b' past the hill over $40 < x < 43$ km. By $x = 42$ km (Fig. 11c) the circulation direction and tendency are reversed from that at $x = 38$ km (Fig. 11b), which leads to renewed upward motion past the hills. This upward motion and its associated decreases in b' over $43 < x < 47$ km are apparent in Figs. 11a,d.

If the parcel at $y = 10$ km remained unsaturated, its lee-wave oscillations would continue as it progressed downstream and its trajectory would resemble that of the Xb40-DRY simulation in Fig. 10c. However, the parcel's lee-wave circulation abruptly ends at $x \approx 47$ km where saturation occurs, N^2 becomes negative, and the phase relationship between ζ and b in (4) reverses. At this point, ζ' and b' at $y = 10$ km are nearly zero, implying that the y-buoyancy gradients that tend to oppose the existing lee-wave circulation are minimal. This is evident in the y–z cross section at $x = 47$ km in Fig. 11d in which the buoyancy anomalies are weak and diffuse compared to those farther upstream (Fig. 11c) and nearly zero above $z = 1$ km. As a consequence, the lee-wave circulation present at saturation continues into the cloud. Now that the parcel is saturated and unstable, farther upward motion causes the buoyancy to *increase* from (4) rather than continue decreasing. Thus b' becomes positive within the updraft at $y = 10$ km, which is apparent in Fig. 11a past $x = 47$ km and in the y–z cross section at $x = 52$ km in Fig. 11e. Now the counterrotating vortices initiated by the lee wave and their tendencies are phase-locked together, which characterizes a convectively amplifying circulation. The continued growth of this circulation, evident in the cross section at $x = 56$ km in Fig. 11f, generates a convective rainband past the hill.

b. VALLEY simulation

The flow dynamics of the VALLEY simulation in Fig. 12 contrast strongly with that in the HILL simulation in Fig. 11. While the unperturbed parcel at $y = 0$ (dashed lines in Fig. 12a) follows a nearly identical relationship between ζ and b as in the HILL case, the perturbation dynamics of the parcel over the valley at $y = 10$ km (solid lines) are much different. This parcel initially descends over the valley, which creates strongly negative ζ' and strongly positive b' over $36 < x < 39$ km in Fig. 12a. This generates ξ tendencies in Fig. 12b that strongly oppose the existing circulation, leading to a phase reversal of the lee wave at $x \approx 39$ km. The parcel ascends and loses buoyancy over $39 < x < 42$ km until saturation occurs at $x \approx 42$ km (Figs. 12a,c), approximately 5 km upstream of that in the HILL simulation. More importantly, saturation occurs at a different phase in the lee wave. Whereas the parcel passing over the hill reached saturation with slightly positive ζ' and slightly negative b', the parcel over the valley saturates with strongly positive ζ' and strongly negative b' (Figs. 12a,c). Thus $\partial b/\partial y$ at cloud entry is much stronger and more concentrated near the y centerpoint of the domain than in the HILL simulation, and its stronger associated vorticity tendencies suppress further upward motion past the valley. By $x = 47$ km (Fig. 12d) the parcel at $y = 10$ km is no longer ascending, but two updrafts are generated in the rising branches of the buoyancy-induced circulation on either side of the valley ($y \approx 7$ km and $y \approx 13$ km). Saturated ascent in these areas leads to positive b' and convective growth, which progressively strengthens as the parcel travels downstream at $x = 52$ km (Fig. 12e) and $x = 56$ km (Fig. 12f). From Figs. 8a,b it is apparent that these cloud bands on the flanks of the valley form slightly farther downstream than the single updraft in the HILL simulation.

c. Xb40 simulation

A similar analysis to that outlined above explains why bands form past the hills and not the valleys in the Xb40 simulation (Fig. 9b). The ζ and b values of air parcels passing over a hill at $y = 10$ km and a valley at $y = 15$ km are shown in Fig. 13a (along with a reference parcel halfway between them at $y = 12.5$ km), indicating the opposite phases of these two parcels prior to saturation. Whereas the parcel at $y = 10$ km rises and loses buoyancy over the hill ($36 < x < 39$ km), the parcel at $y = 15$ km sinks and gains buoyancy over the valley. The b' field at $x = 38$ km in Fig. 13b creates ξ tendencies that reverse the lee-wave circulation, which is apparent in Fig. 13a over $39 < x < 43$ km and in the y–z cross section at $x = 42$ km in Fig. 13c. As in the VALLEY simulation, the parcel traveling past the valleys in Fig. 13a saturates farther upstream with strongly positive ζ' and strongly negative b'. Likewise, this parcel is forced downward and does not rise convectively.
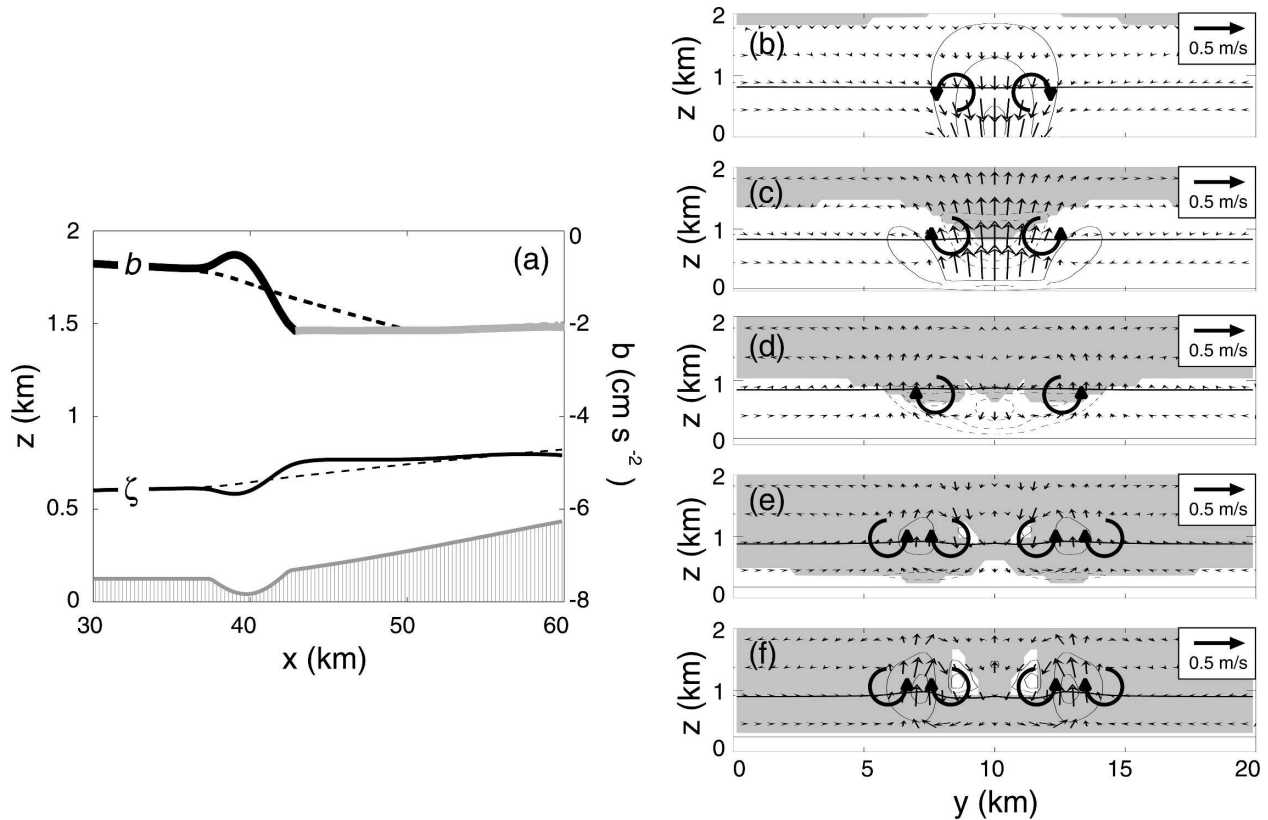
FIG. 12. Same as in Fig. 11, but for VALLEY simulation.

As in the HILL simulation, the parcel at $y = 10$ km saturates at $x \approx 47$ km with $\zeta' \approx 0$ and $b' \approx 0$ (Figs. 13a,d), which allows the existing lee-wave circulation to continue into the cloud. Saturated, unstable ascent causes $b' > 0$ past the hills at $x = 52$ km (Fig. 13e) and the circulation strengthens farther downstream at $x = 56$ km (Fig. 13f).

The series of hills and valleys in the Xb40 simulation (Fig. 13) produces a stronger convective circulation than either the HILL (Fig. 11) or VALLEY (Fig. 12) simulation alone. This is because the regions of $b' > 0$ past the hills are surrounded by $b' < 0$ past the valleys, which increases the strength and scale of the circulation beyond that produced by an isolated feature. As a consequence, the Xb40 simulation exhibits stronger upward motion and more rapid increase of b' past the hills than in the HILL simulation, as well as stronger downward motion and desaturation past the valleys than in the VALLEY simulation. Moreover, the faster initial growth of the convective elements leads to stronger suppression of any convective cells developing between the bands. For example, the two strong bands on the flanks of the valley in the VALLEY simulation, which emerged slightly farther downstream than the single band in the HILL simulation, are unable to develop in the face of strong compensating subsidence from the updrafts on either side. In addition, the enhanced descent past the valleys apparent in Fig. 13d causes low-level desaturation and positive buoyancy anomalies at $x = 52$ km (Fig. 13e) that tend to reverse the sinking motion in these areas. This shallow lee wave causes uplift and resaturation by $x = 56$ km (Fig. 13f), but again the growth of this cloud is suppressed by the subsiding environment in which it develops.

The dynamics of the Xb40 simulation, and of the triggering process in general, may be more easily visualized by the 3D plot of the $q_c = 0.05$ g kg^{-1} contour (light blue surface) and parcel trajectories at $y = 10$ km and $y = 15$ km that are colorized to indicate the sign of b' in Fig. 14. The 3D structure of the orographic cloud demonstrates that saturation first occurs past the valley at $y = 15$ km, but the cloud does not immediately experience convective growth. This is because the large lee-wave displacements in that region create strongly negative b', which leads to sinking motion and desaturation past the cloud leading edge. At $y = 10$ km, the flow saturates with $b' \approx 0$ and consequently continues its saturated, unstable ascent into a convective updraft.
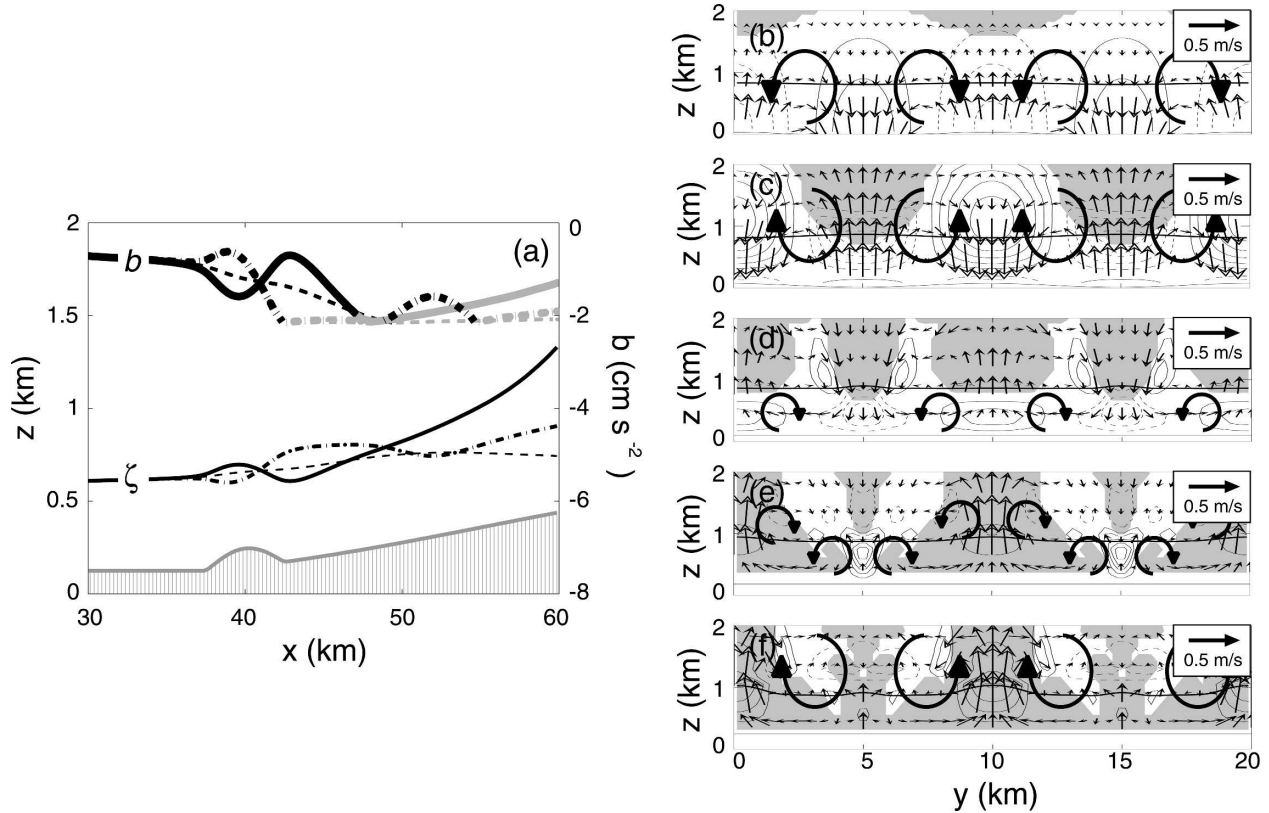
FIG. 13. Same as in Fig. 11, but for Xb40 simulation. (a) The parcel at $y = 10$ km is the solid line, the parcel at $y = 12.5$ km is the dashed line, and the parcel at $y = 15$ km is the dashed–dotted line.

d. A condition for lee-wave triggering

The insight into band formation provided in Figs. 11–13 may be condensed into a simple condition that determines whether an oscillating air parcel will amplify into a band—or sink and desaturate—upon entering the orographic cloud. As seen in Figs. 11–13, air parcels tend to saturate with positive lee-wave-induced vertical velocity perturbations $w' = U \partial \zeta' / \partial_x > 0$. Although such parcels become unstable upon cloud entry, they do not necessarily continue to rise into a convective updraft because they may also possess a negative lee-wave-induced buoyancy perturbation ($b' < 0$), which tends to make them sink. For the idealized simulations of this section, in which air parcels encounter only one small-scale obstacle prior to saturation, the necessary relationship between w' and b' at cloud entry for a band to be triggered is found by considering the vertical momentum and thermodynamic equations for an air parcel:

$$\frac{dw'}{dt} = b' \quad \text{and} \tag{6}$$

$$\frac{db'}{dt} = -N_m^2 w', \tag{7}$$

where $N_m^2 < 0$ is the moist stability of the cloud. These may be combined into a single second-order ordinary differential equation:

$$\frac{d^2 w'}{dt^2} + N_m^2 w' = 0, \tag{8}$$

which, given the initial conditions $w_c = w'(t_c)$ and $b_c = dw'/dt|_{t_c}$, where the parcel arrives at the cloud edge at $t = t_c$, has the solution

$$w'(t) = \frac{1}{2}\left(w_c + \frac{b_c}{|N_m|}\right)e^{|N_m|(t-t_c)}$$

$$+ \frac{1}{2}\left(w_c - \frac{b_c}{|N_m|}\right)e^{-|N_m|(t-t_c)} \quad \text{for}$$

$$t \geq t_c. \tag{9}$$

Assuming that perturbations enter the cloud with positive w_c, the criteria for bandedness is simply that a rising parcel will continue to rise after becoming saturated. This is implemented by setting $w' > 0$ in (9) and neglecting the exponentially decaying term, which yields the relation
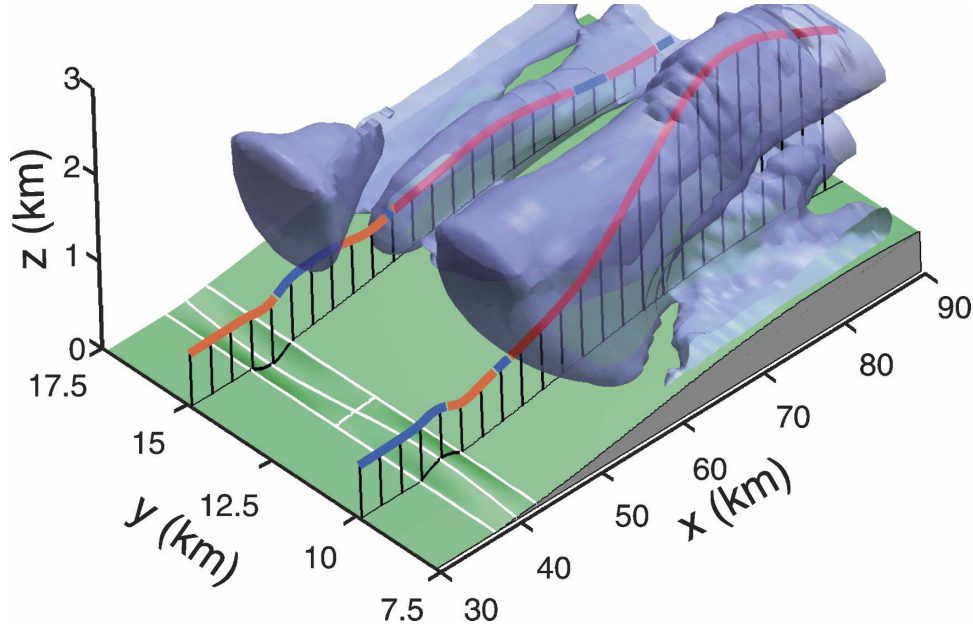
FIG. 14. Three-dimensional diagram of band formation in the Xb40 simulation. The underlying terrain is green, and the $q_c = 0.05$ g kg^{-1} contour is light blue. Parcel trajectories at $y = 10$ km and $y = 15$ km overlaid on these fields are red (blue) when the parcel's buoyancy is positive (negative) relative to the nodal line at $y = 12.5$ km.

$$w_c + \frac{b_c}{|N_m|} > 0. \tag{10}$$

This suggests that bands always form when w_c and b_c are both positive and that bands never form when they are both negative. Positive values of w_c may also produce bands when b_c is slightly negative or greater, provided that w_c is large enough for the parcel to overcome the negative buoyancy that it accumulated in its lee-wave oscillations prior to saturation. The necessary relationship between w_c and b_c in (10) may be used to develop a simple condition on the phase ϕ of a parcel's lee-wave oscillation as it enters the cloud. This is shown by substituting (6) into (10) and assuming that, like $\tilde{h}$, w' prior to saturation follows a sinusoidal pattern given by

$$w'(t) = w_0 \cos[\omega(t - t_c) + \phi] \quad \text{for} \quad t \leq t_c, \tag{11}$$

where $\omega = Uk$ and $k = 2\pi/\lambda_b$ is the dominant wavenumber in the small-scale topography. Using (11) and evaluating (10) at $t = t_c$ gives the condition
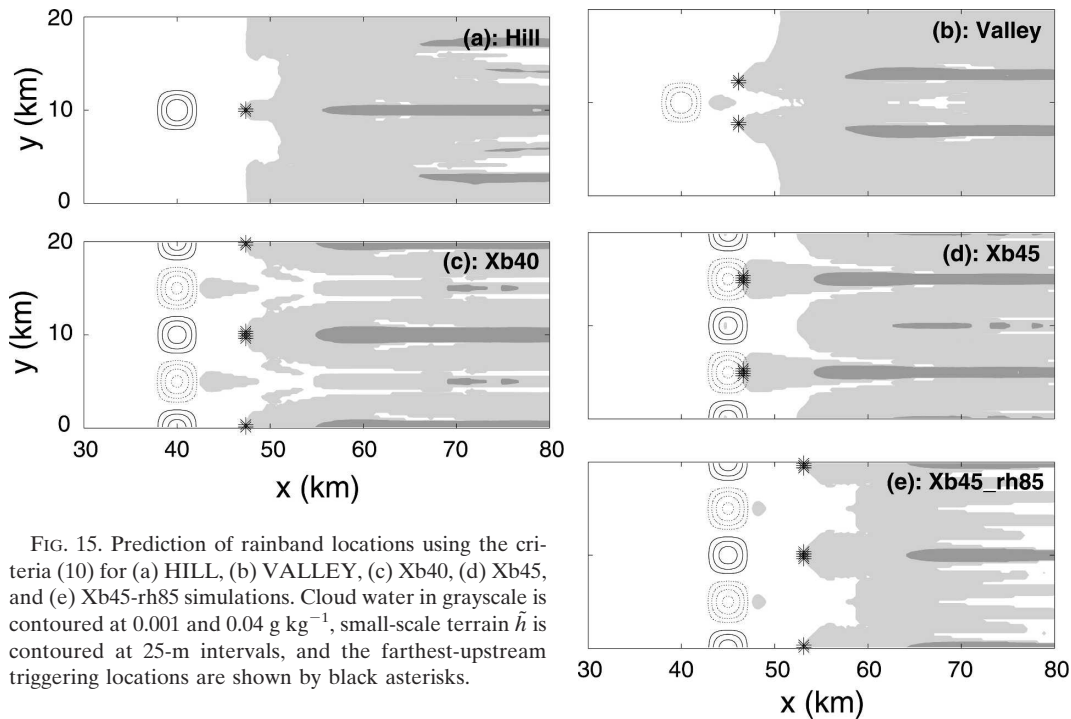
$$\tan\phi < \frac{|N_m|}{Uk} \quad \text{for} \quad w_c > 0. \tag{12}$$

The potential for bandedness thus depends only on ϕ and relevant atmospheric and terrain-related parameters. For the simulations in this paper in which $w_c > 0$

$(-90 \leq \phi \leq 90°)$, this criteria is satisfied only when $-90 < \phi \leq 26°$, which corresponds to just slightly negative b_c and strongly positive w_c ($0 \leq \phi < 26°$) or positive values of both w_c and b_c ($-90 \leq \phi \leq 0°$).

This theory is evaluated in Figs. 15a–c, in which shaded contours of q_c in the HILL, VALLEY, and Xb40 simulations are overlaid by the farthest-upstream points where (10) is satisfied. In all three cases, satisfaction of (10) (shown by the black asterisks) accurately predicts the leading edges of bands that, farther downstream, generate high values of q_c and darker contours. Note that for this calculation U and N_m^2 are again given by representative values of 10 m s^{-1} and -1.5×10^{-5} s^{-2} (the latter estimated from Fig. 7b). In addition, only the upstream-most triggering points are shown because the complexity of the flow after bands are initiated cannot be described by this simplified parcel theory.
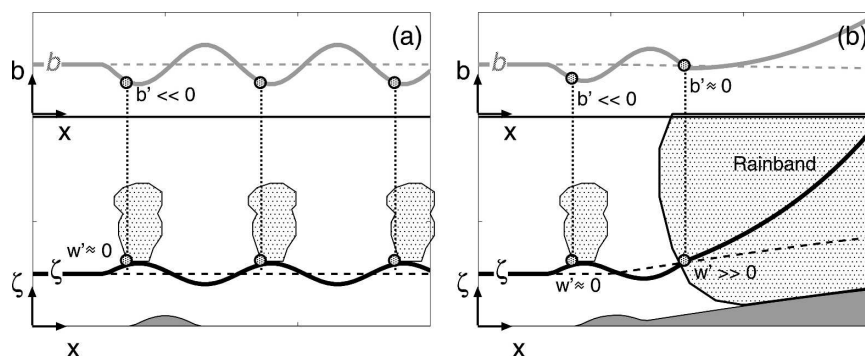
From (10) it readily follows that in weakly moist unstable environments like those in this study, rainbands form more easily over the upslope of a mesoscale ridge than over a nonsloping surface. This is illustrated by the schematic diagram in Fig. 16. Over a nonsloping surface (Fig. 16a), unsaturated parcels require a finite amount of lee-wave displacement ζ_c to reach saturation, and as a result b_c tends to be negative at cloud entry. When $|N_m|$ is small, this negative b_c strongly resists convective growth and may force the air to subside and desaturate. Such nonconvective clouds may also develop over a

FIG. 15. Prediction of rainband locations using the criteria (10) for (a) HILL, (b) VALLEY, (c) Xb40, (d) Xb45, and (e) Xb45-rh85 simulations. Cloud water in grayscale is contoured at 0.001 and 0.04 g kg^{-1}, small-scale terrain $\tilde{h}$ is contoured at 25-m intervals, and the farthest-upstream triggering locations are shown by black asterisks.

sloping surface (Fig. 16b) when a lee-wave updraft like that at $x \approx 38$ km is positioned well upstream of the nominal cloud edge. However, as the air advances up the hill, it becomes progressively more humid and the amount of lee-wave-induced displacement necessary for it to saturate decreases. This allows the oscillating lee wave to resaturate with strongly positive w_c yet nearly zero ζ_c and b_c, which from (10) is a more conducive combination for band triggering. Note that in more unstable environments with larger $|N_m|$, the suppressive effects of negative b_c are diminished in (10) and rising air parcels are more likely to continue their ascent after saturating.

6. Sensitivity of rainband locations

The phases of small-scale lee waves at saturation, and thus the locations of orographic rainbands, strongly depend on both atmospheric and terrain-related parameters over a range of horizontal scales. For example, the vertical structures of the lee waves upstream of the orographic cloud are determined not only by $\tilde{h}$, but by the wind speed U and static stability N_d^2 of the large-scale impinging flow. The location at which the flow saturates also depends on parameters in the upstream sounding profile (e.g., U, N_d^2, and RH), as well as the shape of the ridge $\bar{h}$ and the small-scale features $\tilde{h}$ em-

FIG. 16. Schematic diagram of the differences in cloud formation between (a) nonsloping and (b) upward-sloping terrain in marginally conditionally unstable flow over a small-scale hill.
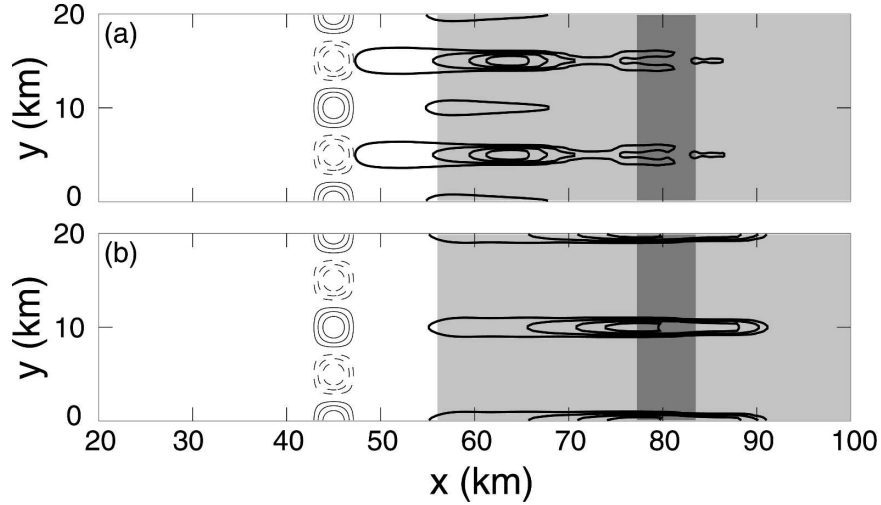
FIG. 17. Same as in Fig. 9 but for (a) Xb45 and (b) Xb45-RH85 simulations.

bedded upon it. The sensitivity of rainband locations to parameters on both small and large scales is demonstrated through two simulations (Xb45 and Xb45-RH85) that are identical to the Xb40 case in Fig. 9b except that $x_b = 45$ km and, in the Xb45-RH85 simulation, the relative humidity at low levels ($0 \leq z \leq 5$ km) is lowered from 90% to 85%. To maintain a similar degree of potential instability as the original sounding, the surface temperature in the Xb45-RH85 simulation is increased from 285 to 286 K.

As in the Xb40 case (Fig. 9b), the q_c field of the Xb45 simulation (Fig. 17a) exhibits two dominant orographic rainbands. However, instead of lying downstream of the two hills in $\tilde{h}$, the bands are now located downstream of the two valleys, reinforcing the idea that both hills and valleys are capable of triggering bands. Plots of ζ and b at $y = 10$ km (between bands) and at $y = 15$ km (along a band) in Fig. 18a reveal that, with x_b now farther downstream, the strip of nonzero $\tilde{h}$ lies much closer to the leading edge of the cloud. As a result, the ascending flow over the hill at $y = 10$ km saturates earlier ($x \approx 43$ km) than that over the valley at $y = 15$ km ($x \approx 47$ km). However, the parcel over the hill saturates with $w_c \approx 0$ and $b_c \ll 0$, a nonconducive combination for the triggering of convection. This is illustrated in Fig. 15d, where the initial triggering points found from (10) are past the valleys rather than the hills. The parcel traveling over the valley saturates with strongly positive w_c and $b_c \approx 0$ ($\phi \approx 0°$), a more favorable cloud-entry phase that satisfies (10) and leads to convective growth downstream.

The influence of larger-scale flow parameters on rainband location is demonstrated by the q_c field of the Xb45-RH85 simulation (Fig. 17b), in which the bands

return to the same locations relative to the hills as in the Xb40 case. This small reduction in moisture increases the amount of upward displacement necessary for saturation, which consequently alters the nominal cloud location and in turn the phase of the small-scale lee waves
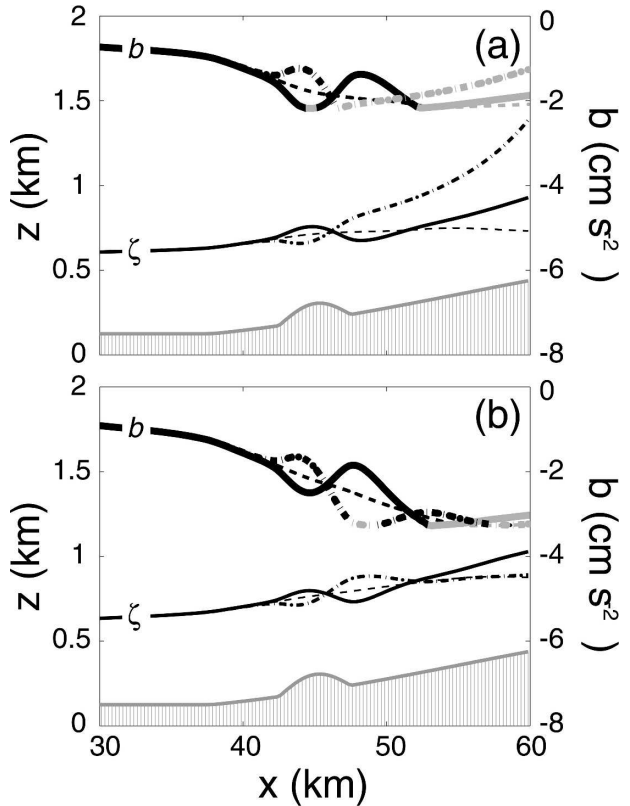

FIG. 18. Same as in Fig. 11a, but for (a) Xb45 and (b) Xb45-RH85 simulations.

at cloud entry. This is shown in Fig. 18b, where the parcel over the hill experiences oscillations until saturating at $x \approx 52$ km, while the parcel over the valley saturates at $x \approx 47$ km. In this case, the parcels traveling past the valleys have strongly negative b_c and weakly positive w_c, which from (10) is not conducive for band triggering. The parcels past the hills have just slightly negative b_c and nearly maximum w_c, which satisfies (10) and leads to band formation past the small-scale hills (Fig. 15e).

7. Conclusions

An observational and numerical investigation into the triggering of convective orographic rainbands by small-scale topographic obstacles has been presented. Radar observations of quasi-stationary rainbands in one event over the Coastal Range in western Oregon are accurately reproduced by a quasi-idealized simulation of the event that uses realistic representations of the upstream flow conditions and the Coastal Range terrain. The simulated bands have similar locations and structures as those in the radar data, indicating that the simulation accurately captures the key dynamical processes leading to band formation.

The numerical simulations are progressively simplified to address the influence of both environmental and terrain-related parameters on band formation. Idealized simulations with uniform wind profiles indicate that the rainbands do not require background vertical shear to develop, and that they tend to align parallel to the low-level flow direction. Simulations with simplified terrain profiles reveal several important aspects of orographic convection, including 1) the small-scale terrain over a limited area just upstream of the leading edge of the orographic cap cloud dictates the convective signature, 2) both small-scale hills and valleys are able to trigger bands, and 3) the locations where rainbands form are very sensitive to large-scale flow conditions and the position of small-scale topographic features relative to the cloud leading edge.

The dynamics by which orographic rainbands are triggered by small-scale topographic obstacles are summarized as follows. As the moist impinging flow is lifted en masse toward saturation by the smooth mesoscale ridge $\overline{h}(x)$, embedded small-scale terrain features on the mountain $\tilde{h}(x, y)$ generate lee waves that impose y variability on the flow and perturb the leading edge of the orographic cap cloud. Whether a given small-scale feature generates a band depends on the phase of its lee wave at saturation. Only when the lee-wave-induced vertical velocity perturbation w_c is strongly positive and its buoyancy perturbation b_c is slightly negative or greater does a band develop past a given obstacle.

Through simple parcel analysis a threshold condition for band triggering is derived that accurately determines the band locations based on w_c, b_c, and the Brunt–Väisälä frequency inside the cloud N_m.

This threshold relationship between w_c and b_c may be understood by considering the dynamics of airflow at the leading cloud edge. Oscillating air parcels tend to saturate with positive w_c and ζ_c, the latter of which implies negative buoyancy accumulation ($b_c < 0$) in the statically stable flow upstream of the cloud. Upon entering the unstable cloud, the phase relationship between w_c and b_c reverses, causing parcels to warm as they continue to ascend. This unstable upward motion does not always lead to convective growth because an initially cold parcel will ultimately sink and desaturate if it stays cold relative to its surroundings (i.e., if its buoyancy anomaly remains negative). Convection thus develops only when w_c is sufficiently large for the parcel to overcome its negative b_c and become positively buoyant, after which it ascends into an updraft core as it moves downstream.

A full picture of the dynamics of orographic rainbands requires a physical understanding of not just the band formation process but also the preferred spatial scales of the bands. The latter is a complex issue that is addressed in a follow-on study currently underway that, like this study, uses a combination of numerical simulations and analytical theory. Because the theories developed here are based on just a single event over the Coastal Range, future efforts will also focus on applying these concepts to other cases of banded orographic convection over the Coastal Range, as well as to banded convection over other mountain ranges around the world.

REFERENCES

Bryan, G. H., and J. M. Fritsch, 2002: A benchmark simulation for moist nonhydrostatic models. *Mon. Wea. Rev.,* **130,** 2917–2928.

Cosma, S., E. Richard, and F. Miniscloux, 2002: The role of small-scale orographic features in the spatial distribution of precipitation. *Quart. J. Roy. Meteor. Soc.,* **128,** 75–92.

Dirks, R. A., 1973: The precipitation efficiency of orographic clouds. *J. Rech. Atmos.,* **7,** 177–184.

Douglas, R. H., 1964: Hail size distributions. *Proc. Conf. on Radio*

Meteorology and 11th Weather Radar Conf., Boulder, CO, Amer. Meteor. Soc., 146–149.

Durran, D. R., and J. B. Klemp, 1982: On the effects of moisture on the Brunt–Väisälä frequency. *J. Atmos. Sci.,* **39,** 2152–2158.

——, and ——, 1983: A compressible model for the simulation of moist mountain waves. *Mon. Wea. Rev.,* **111,** 2341–2361.

Elliott, R. D., and E. L. Hovind, 1964: The water balance of orographic clouds. *J. Appl. Meteor.,* **3,** 235–239.

Fuhrer, O., and C. Schär, 2005: Embedded cellular convection in moist flow past topography. *J. Atmos. Sci.,* **62,** 2810–2828.

Houze, R. A., 1993: *Cloud Dynamics.* Academic Press, 573 pp.

Kirshbaum, D. J., and D. R. Durran, 2004: Factors governing cellular convection in orographic precipitation. *J. Atmos. Sci.,* **61,** 682–698.

——, and ——, 2005a: Atmospheric factors governing banded orographic convection. *J. Atmos. Sci.,* **62,** 3758–3774.

——, and ——, 2005b: Observations and modeling of banded orographic convection. *J. Atmos. Sci.,* **62,** 1463–1479.

Klemp, J. B., and R. Wilhelmson, 1978: The simulation of three-dimensional convective storm dynamics. *J. Atmos. Sci.,* **35,** 1070–1096.

Lilly, D. K., 1962: On the numerical simulation of buoyant convection. *Tellus,* **14,** 148–172.

Miniscloux, F., J. D. Creutin, and S. Anquetin, 2001: Geostatistical analysis of orographic rainbands. *J. Appl. Meteor.,* **40,** 1835–1854.

Wicker, L. J., and W. C. Skamarock, 2002: Time splitting methods for elastic models using forward time schemes. *Mon. Wea. Rev.,* **130,** 2088–2097.

Yoshizaki, M., T. Kato, Y. Tanaka, H. Takayama, Y. Shoji, and H. Seko, 2000: Analytical and numerical study of the 26 June 1998 orographic rainband observed in western Kyushu, Japan. *J. Meteor. Soc. Japan,* **78,** 835–856.